

# Quantifying the efficiency of principal signal transmission modes in proteins

Anil Kumar Sahoo,<sup>1,2</sup> Richard Schwarzl,<sup>1</sup> Markus S. Miettinen,<sup>1,\*</sup> and Roland R. Netz<sup>1,3,†</sup>

<sup>1</sup>*Fachbereich Physik, Freie Universität Berlin, Arnimallee 14, 14195 Berlin, Germany*

<sup>2</sup>*Max Planck Institute of Colloids and Interfaces, Am Mühlenberg 1, 14476 Potsdam, Germany*

<sup>3</sup>*Centre for Condensed Matter Theory, Department of Physics,  
Indian Institute of Science, Bangalore 560012, India*

On the microscopic level, biological signal transmission relies on coordinated structural changes in allosteric proteins that involve sensor and effector modules. The timescales and microscopic details of signal transmission in proteins are often unclear, despite a plethora of structural information on signaling proteins. Based on linear-response theory, we develop a theoretical framework to define frequency-dependent force and displacement transmit functions through proteins and, more generally, viscoelastic media. Transmit functions quantify the fraction of a local time-dependent perturbation at one site, be it a deformation, a force or a combination thereof, that survives at a second site. They are defined in terms of equilibrium fluctuations from simulations or experimental observations. We apply the framework to our all-atom molecular dynamics simulation data of a parallel, homodimeric coiled-coil (CC) motif that connects the sensor and effector modules of a blue-light-regulated histidine kinase from bacterial signaling systems extensively studied in experiments. Our analysis reveals that signal transmission through the CC is possible via shift, splay, and twist deformation modes. Based on results of mutation experiments, we infer that the most relevant mode for the biological function of the histidine kinase protein is the splay deformation.

Keywords: protein, allostery, coiled coil, signal transfer, response function, molecular simulation

## INTRODUCTION

Signal transmission within a cell, between cells, and from the exterior to the interior of a cell is necessary for any form of life, be it bacteria, plants, or animals. Signal-transducing units, at the molecular level, involve signal receptors (sensors) that sense intracellular or environmental changes (such as photons, hormones or pH) and corresponding effectors that are responsible for sparking a response [1, 2]. Sensor and effector modules are usually distinct domains of membrane-bound or cytosolic proteins [3–5]. How information, at the molecular level, is transmitted through proteins has been subject of intense research in the last few decades [6–14]. Experimental techniques, such as NMR spectroscopy [15, 16], time-resolved crystallography [17, 18], cryo-electron microscopy [19], and single-molecule experiments [20–22] have provided information about protein structure, dynamics, and mechanical signaling pathways. Computational approaches combining molecular simulation techniques [23–27] and tools from information theory [28] and graph theory [29–31], along with various linear or non-linear correlation analyses [32, 33], have provided molecular-level insights into protein allosteric communication pathways [34, 35]. A combination of spectroscopy techniques and molecular dynamics

(MD) simulation description has led to recent insights into time-resolved processes of allosteric regulation [36–41]. However, the quantitative relation between the dynamics of a protein and its signal transfer efficacy, which ultimately governs physiological response, is missing.

We here show how to quantify the signal-transfer efficiency through proteins in terms of frequency-dependent force and displacement transmit functions. A force transmit function describes the fraction of the frequency-dependent force applied at the protein sensor position that survives at the effector position. The displacement transmit function is defined similarly but is based on spatial displacements. In fact, the presence of strongly correlated fluctuations at the sensor and effector positions, as quantified by two-point correlation functions, is not sufficient for efficient signal transmission, because equilibrium fluctuations produce a background that the signal has to compete with. Transmit functions weigh the correlation between the sensor and effector positions by the fluctuation magnitude and therefore quantify the fractional signal transmission, they are thus very different from ordinary two-point correlation functions. Our theoretical framework builds on our previously developed convolution theory [42] and is exact on the linear-response level [43]. From the time-domain transmit function, the protein response to any temporal perturbation signal can be calculated by convolution, all one needs as input to our theory are time series of positions or displacements that can be obtained from MD simulations or single-molecule experiments, e.g., by fluorescence resonance energy transfer [20].

Here, we focus on coiled-coil motifs, frequently found

\* Present address: Computational Biology Unit, Departments of Chemistry and Informatics, University of Bergen, 5007 Bergen, Norway

† rnetz@physik.fu-berlin.de

in various plant and bacterial signal transduction systems, that connect signal receptor and response or effector protein [4, 44–50]. Signal receptors are commonly oligomeric domains and modular in architecture, produced by recombination of sensor and effector modules. Signaling through coiled coils leads to conformational rearrangements within effectors that trigger interaction with regulator proteins, starting signaling cascades. Studies investigating the role of coiled coils in signal propagation are, however, limited to quantifying their structural changes in the presence of an external signal, e.g., pivoting or rotation of the helices [19, 50].

We perform all-atom MD simulations of a coiled-coil (CC) motif consisting of two identical  $\alpha$ -helices arranged in parallel that is part of an engineered blue-light-regulated histidine kinase [51]. In this synthetic enzyme, the CC connects the light-oxygen-voltage sensor module from *Bacillus subtilis* YtvA and the histidine kinase complex from the bacterium *Bradyrhizobium japonicum*, see Fig. 1A. We study the dynamics of the isolated CC in terms of its shift, splay, and twist deformation modes. Computed transmit functions reveal that all modes are able to transmit signals. From the time-domain transmit functions we derive transmit properties of different time-dependent signals. For step signals we find that transmission via the splay mode is drastically reduced by single-point mutations in the CC, whereas the twist mode is least affected. Together with the experimental observation of light-induced splaying of the CC [17, 52] and experimental mutation studies [5], this suggests that splay is the most relevant deformation mode of the CC for the biological function of this sensor histidine kinase [51].

## RESULTS

### A. Theory of transmit functions

The input–output relation for a general responsive system can be quantified by two transmit functions: force and displacement transmission. Consider we apply to a system’s sensor (input) position a frequency-dependent force  $\tilde{F}_s(\omega)$  and to its effector (output) position a force  $\tilde{F}_e(\omega)$ , see Fig. 1B. In Fourier space, the sensor and effector positions change as [42]

$$\begin{aligned}\tilde{X}_s(\omega) &= \tilde{J}_{\text{self}}^s(\omega)\tilde{F}_s(\omega) + \tilde{J}_{\text{cross}}(\omega)\tilde{F}_e(\omega) \\ \tilde{X}_e(\omega) &= \tilde{J}_{\text{self}}^e(\omega)\tilde{F}_e(\omega) + \tilde{J}_{\text{cross}}(\omega)\tilde{F}_s(\omega),\end{aligned}\quad (1)$$

where  $\tilde{J}_{\text{cross}}(\omega)$  and  $\tilde{J}_{\text{self}}^{s/e}(\omega)$  are the frequency-dependent cross and self (sensor/effector-side) linear response functions, respectively. Note that there is only a single cross-response. However, the self-responses

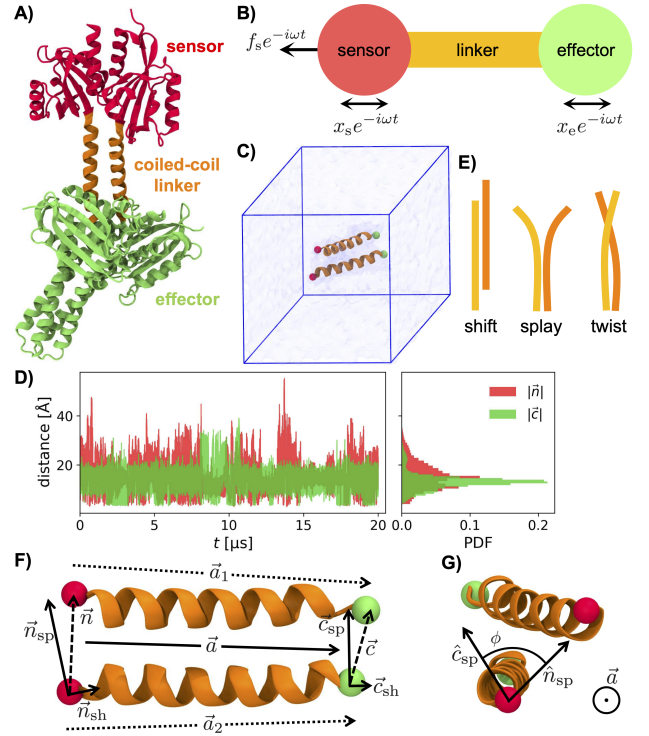


Figure 1. A) The full-length structure of the dark-adapted blue-light-regulated histidine kinase YF1 (PDB ID: 4GCZ) [53]. In YF1 the sensor, linker, and effector modules are homodimeric at the molecular level. B) Schematic representation of signal transmission from sensor to effector sites. C) Simulation unit cell containing the coiled-coil (CC) linker. Water and ions are not shown. D) Time series and corresponding probability density functions (PDFs) for the N and C-termini distances of the CC,  $|\vec{n}|$  and  $|\vec{c}|$ . E) Schematic representation of shift, splay, and twist modes of the CC. F) Schematics for defining the shift vectors  $\vec{n}_{\text{sh}}$ ,  $\vec{c}_{\text{sh}}$  and the splay vectors  $\vec{n}_{\text{sp}}$ ,  $\vec{c}_{\text{sp}}$  as the parallel and perpendicular components of the distance vectors  $\vec{n}$ ,  $\vec{c}$  with respect to the symmetrized CC axis  $\vec{a} = (\vec{a}_1 + \vec{a}_2)/2$ . G) Schematic for describing twist as rotation of splay unit vectors  $\hat{n}_{\text{sp}}$  and  $\hat{c}_{\text{sp}}$  around the long-axis  $\vec{a}$ . The angle between  $\hat{n}_{\text{sp}}$  and  $\hat{c}_{\text{sp}}$  is denoted as the twist angle  $\phi$ .

$\tilde{J}_{\text{self}}^s(\omega)$  and  $\tilde{J}_{\text{self}}^e(\omega)$  are different for a general asymmetric system. It should be further noted that Eq. 1 is exact on the linear response level and is applicable for any two positions in a protein. The force transmit function  $\tilde{T}_{\text{F}}^{s \rightarrow e}(\omega)$  is defined for the boundary condition of a stationary effector position  $\tilde{X}_e = 0$ , from Eq. 1, we obtain

$$\tilde{T}_{\text{F}}^{s \rightarrow e}(\omega) \equiv \frac{\tilde{F}_e(\omega)}{-\tilde{F}_s(\omega)} = \frac{\tilde{J}_{\text{cross}}(\omega)}{\tilde{J}_{\text{self}}^e(\omega)}.\quad (2)$$

Similarly, setting  $\tilde{X}_s = 0$  in Eq. 1, we obtain  $\tilde{T}_{\text{F}}^{e \rightarrow s} \equiv$

$-\tilde{F}_s/\tilde{F}_e = \tilde{J}_{\text{cross}}/\tilde{J}_{\text{self}}^s$ . Response functions are *causal*, i.e., there is no positional response before a force is applied, which implies  $\tilde{J}_{\text{cross}}(\omega)$  and  $\tilde{J}_{\text{self}}(\omega)$  are analytic in the upper-half complex plane. If furthermore  $\tilde{J}_{\text{self}}(\omega)$  is non-zero in the upper-half complex plane, from Eq. 2 it follows that transmit functions are also causal.

The displacement transmit function  $\tilde{T}_X^{\text{s}\rightarrow\text{e}}(\omega)$  is defined as the ratio of the displacement of the effector site  $\tilde{X}_e$  divided by the displacement at the sensor site  $\tilde{X}_s$  under force-free boundary condition  $\tilde{F}_e = 0$ . Inverting Eq. 1 yields

$$\begin{aligned} \begin{pmatrix} \tilde{F}_s \\ \tilde{F}_e \end{pmatrix} &= \frac{1}{\tilde{J}_{\text{self}}^s \tilde{J}_{\text{self}}^e - \tilde{J}_{\text{cross}}^2} \begin{pmatrix} \tilde{J}_{\text{self}}^e & -\tilde{J}_{\text{cross}} \\ -\tilde{J}_{\text{cross}} & \tilde{J}_{\text{self}}^s \end{pmatrix} \begin{pmatrix} \tilde{X}_s \\ \tilde{X}_e \end{pmatrix} \\ &= \begin{pmatrix} \tilde{G}_{\text{self}}^s & \tilde{G}_{\text{cross}} \\ \tilde{G}_{\text{cross}} & \tilde{G}_{\text{self}}^e \end{pmatrix} \begin{pmatrix} \tilde{X}_s \\ \tilde{X}_e \end{pmatrix}, \end{aligned} \quad (3)$$

where  $\tilde{G}$ 's are the moduli determined by inverting the response matrix  $\begin{pmatrix} \tilde{J}_{\text{self}}^s & \tilde{J}_{\text{cross}} \\ \tilde{J}_{\text{cross}} & \tilde{J}_{\text{self}}^e \end{pmatrix}$ . From Eq. 3 we obtain

$$\tilde{T}_X^{\text{s}\rightarrow\text{e}} \equiv \frac{\tilde{X}_e}{\tilde{X}_s} = \frac{-\tilde{G}_{\text{cross}}}{\tilde{G}_{\text{self}}^e} = \frac{\tilde{J}_{\text{cross}}}{\tilde{J}_{\text{self}}^s} = \tilde{T}_F^{\text{e}\rightarrow\text{s}} \quad (4)$$

and by setting  $\tilde{F}_s = 0$  similarly  $\tilde{T}_X^{\text{e}\rightarrow\text{s}} \equiv \tilde{X}_s/\tilde{X}_e = \tilde{T}_F^{\text{s}\rightarrow\text{e}}$ . Thus, force and inverse displacement transmit functions are the same. Note the striking resemblance between transmit functions defined here and the transfer function which characterizes the output of a linear time-invariant system (e.g., an electric circuit consisting of resistors, inductors and capacitors) in the context of signal processing [54].

In practice, one need not apply external forces to determine linear response functions.  $J(t)$  can be obtained from equilibrium time-correlation functions  $C(t)$  using the fluctuation-dissipation theorem [43]:

$$J(t) = -\frac{1}{k_B T} \theta(t) \frac{d}{dt} C(t), \quad (5)$$

where  $k_B$  is the Boltzmann's constant,  $T$  represents temperature, and  $\theta(t)$  is the Heaviside step function. The needed cross and self correlation functions are defined as  $C_{\text{cross}}(t) = \langle X_s(0)X_e(t) \rangle$  and  $C_{\text{self}}^s(t) = \langle X_s(0)X_s(t) \rangle$ ,  $C_{\text{self}}^e(t) = \langle X_e(0)X_e(t) \rangle$ , respectively (see *Materials and Methods* for details). Note that the trajectories of the positions of two sites in a protein needed for the calculation of  $C(t)$  can be obtained from MD simulations but also from single-molecule experiments [20].

## B. MD simulations of the CC linker

We consider the bacterial signaling protein introduced above to demonstrate the applicability of our theoretical framework to real systems. The water-soluble

structure of the whole protein (Fig. 1A) is too large to carry out simulations for a sufficiently long time. Also, we are primarily interested in the CC because of its relevance in diverse signal receptors [4, 44, 46, 50] and of the availability of structural and experimental data [5, 17, 51–53, 55]. We therefore perform explicit solvent all-atom MD simulations of only the CC linker excluding the sensor and effector modules. A summary of simulation details is given in *Materials and Methods* and the simulation unit cell is shown in Fig. 1C. We find that the distribution of the N-termini distance at the sensor side is broader compared to the C-termini distance at the effector side, both distributions exhibit tails that reflect intermittent splaying of the  $\alpha$ -helix termini (see Fig. 1D,E). To check the long-time stability of secondary and tertiary structures of the CC, we calculate three different order parameters: the fraction of native contacts  $Q$  between the two  $\alpha$ -helices, the root-mean-square deviation (RMSD) of distances between the native and simulated CC structures, the former taken from the crystal structure of the full-length protein shown in Fig. 1A, and the secondary structure (SS) content. These order parameters are defined in *SI Appendix*, section 1 and their time-averaged values are given in *SI Appendix*, Fig. S1. The overall configuration of the CC remains stable within 20  $\mu\text{s}$  of simulation as indicated by an average RMSD of 2.5  $\text{\AA}$ . The two  $\alpha$ -helices remain bound to each other ( $Q = 0.92$ ) due to salt bridges (involving residues Arg<sup>135</sup> and Glu<sup>138,142</sup>) and hydrophobic interactions (involving residues Leu<sup>136,139,143</sup> and Val<sup>146</sup>) [5, 53]. Individual  $\alpha$ -helices do not melt as their fraction of SS content values is above 0.85.

## C. The CC linker transmits signals via shift, splay and twist modes

We consider the CC linker deformations that correspond to forces of equal magnitude and opposite direction acting on the two N-termini and on the two C-termini. Thus, these deformations conserve linear momentum. We define three distinct deformation modes by the orientation of the terminal displacement vector with respect to the distance vector between the terminal groups: splay, where the displacement is parallel to the terminal separation, and shift and twist, where the displacement is perpendicular to the terminal separation, see schematics in Fig. 1E. Splay conserves angular momentum, whereas shift and twist do not and are counteracted by a rotation of the sensor module. Since the typical rotational diffusion time of the sensor module, estimated to be of the order of 1  $\mu\text{s}$  (see *Materials and Methods*), is much longer than shift and twist relaxation times, as will be shown below, shift and twist modes are nevertheless possible signal transmission modes.

The three signal transmission modes are obtained as

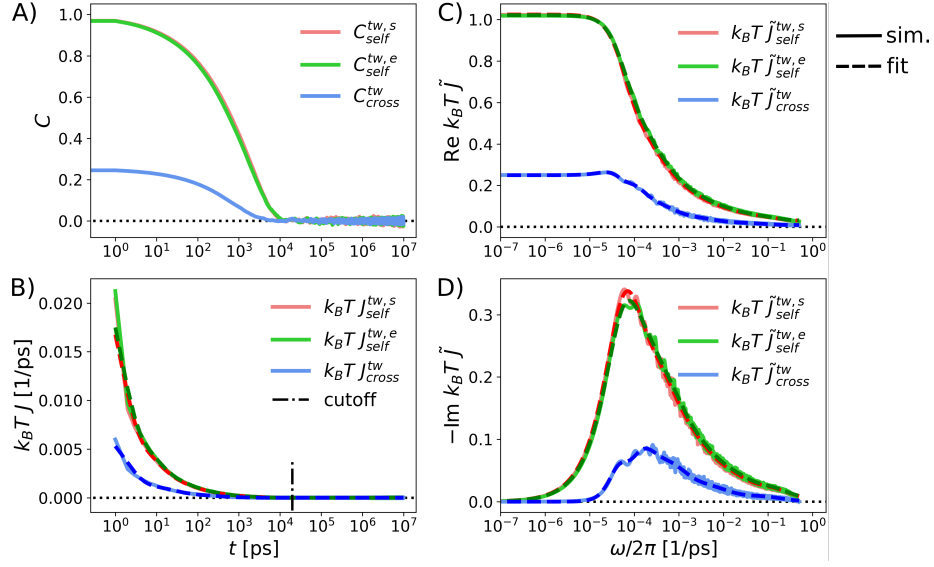


Figure 2. A) Self and cross-correlation functions ( $C_{\text{self}}$  and  $C_{\text{cross}}$ ) for the twist mode of the CC. B) Response functions  $J$ , obtained according to Eq. 5 from numerical derivatives of the correlation functions in A (solid lines). The vertical dash-dotted line represents the cutoff beyond which the response functions are set to zero to prevent noise artifacts when calculating Fourier transforms. C) Real and D) imaginary parts of  $\tilde{J}(\omega)$  obtained from discrete Fourier transform of  $J(t)$  are shown as solid lines. Dashed lines represent simultaneous fits to the real and imaginary parts by a sum of 10 Debye relaxation functions (for further details see *SI Appendix*, section 3). Dashed lines in panel B represent the inverse Fourier transform of the fits in C and D.

described below. The position vectors of the N-termini and C-termini are  $\vec{N}_i$  and  $\vec{C}_i$ , respectively, where  $i = 1, 2$  refers to the first and second  $\alpha$ -helix. These vectors are used to construct the separation vectors  $\vec{c} = \vec{C}_2 - \vec{C}_1$ ,  $\vec{n} = \vec{N}_2 - \vec{N}_1$ , and  $\vec{a}_i = \vec{C}_i - \vec{N}_i$  (Fig. 1F). From the end-to-end vectors  $\vec{a}_i$ , we define the long axis of the CC as  $\vec{a} = (\vec{a}_1 + \vec{a}_2)/2$ . With respect to  $\vec{a}$ , we separate  $\vec{n}$  into the parallel component, shift ( $n_{\text{sh}} = |\vec{n}_{\text{sh}}| = \vec{n} \cdot \hat{a}$ ) and the perpendicular component, splay ( $n_{\text{sp}} = |\vec{n}_{\text{sp}}| = |\vec{n} - \vec{n}_{\text{sh}}|$ ). Similarly, for the C-termini we obtain  $c_{\text{sh}}$  and  $c_{\text{sp}}$ . The twist angle  $\phi$ , depicted in Fig. 1G, is obtained from the scalar product of the two splay unit vectors  $\hat{n}_{\text{sp}}$  and  $\hat{c}_{\text{sp}}$  as  $\phi = \cos^{-1}(\hat{n}_{\text{sp}} \cdot \hat{c}_{\text{sp}})$ . We show time series of these deformation modes and the corresponding probability distribution functions in *SI Appendix*, Fig. S2. Importantly, we find a strong bias towards clockwise rotation of the CC around its long axis  $\vec{a}$ , from the handedness plot obtained from the simulation (see *SI Appendix*, Fig. S2), in agreement with the experimental observation of the left-handed supercoiling of the CC [17].

The N and C-termini of the CC correspond to the sensor (s) and effector (e) side, respectively. For the shift mode, the two self-correlation functions are defined as  $C_{\text{self}}^{\text{sh},s} = \langle n_{\text{sh}}(0)n_{\text{sh}}(t) \rangle$  and  $C_{\text{self}}^{\text{sh},e} = \langle c_{\text{sh}}(0)c_{\text{sh}}(t) \rangle$  and the cross-correlation function is defined as  $C_{\text{cross}}^{\text{sh}} = \langle n_{\text{sh}}(0)c_{\text{sh}}(t) \rangle = \langle c_{\text{sh}}(0)n_{\text{sh}}(t) \rangle$ . Correlation functions

for the splay mode are defined by interchanging the shift quantities with the related splay quantities, e.g.,  $C_{\text{self}}^{\text{sp},s} = \langle n_{\text{sp}}(0)n_{\text{sp}}(t) \rangle$ . For the twist mode, the cross and two self-correlation functions are defined by the scalar product of the splay unit vectors as  $C_{\text{cross}}^{\text{tw}} = \langle \hat{n}_{\text{sp}}(0) \cdot \hat{c}_{\text{sp}}(t) \rangle = \langle \hat{c}_{\text{sp}}(0) \cdot \hat{n}_{\text{sp}}(t) \rangle$  and  $C_{\text{self}}^{\text{tw},s} = \langle \hat{n}_{\text{sp}}(0) \cdot \hat{n}_{\text{sp}}(t) \rangle$  and  $C_{\text{self}}^{\text{tw},e} = \langle \hat{c}_{\text{sp}}(0) \cdot \hat{c}_{\text{sp}}(t) \rangle$ , respectively. To disentangle twist from overall CC rotation, we calculate twist correlation functions in the molecular coordinate frame obtained by removing the CC center-of-mass translation and rigid-body rotation around its principal axes at each time step. We present results for the twist mode in Fig. 2 and for shift and splay modes in *SI Appendix*, Fig. S3. Self and cross-correlation functions are shown in Fig. 2A, the corresponding response functions  $J(t)$ , obtained according to Eq. 5, are shown in Fig. 2B. All self and cross-response functions smoothly decay to zero. The relaxation time, defined as the largest decay time  $\tau_{\text{max}}$  of a multi-exponential fit of  $J$  (*SI Appendix*, section 3), is found to be the fastest for twist ( $\tau_{\text{max}} = 2.6$  ns), followed by shift ( $\tau_{\text{max}} = 7.1$  ns) and splay ( $\tau_{\text{max}} = 9.4$  ns). As expected, for each mode the two self response functions are greater than the cross response at all times. The real and imaginary parts of the Fourier-transformed response functions,  $\text{Re } \tilde{J}(\omega)$  and  $\text{Im } \tilde{J}(\omega)$ , are shown in Fig. 2C,D. There is a distinct low-frequency plateau/peak in the real/imaginary

part of the twist response. To obtain analytical representations, we fit multi-Debye functions (dashed lines) to the Fourier-transformed response functions  $\tilde{J}(\omega)$  in Fig. 2C,D (details are provided in *SI Appendix*, sections 2 and 3). Inverse Fourier transforms of the fit functions (dashed lines) reproduce the time-domain response functions,  $J(t)$ , data shown in Fig. 2B very well.

Force transmit functions,  $\tilde{T}_F(\omega)$ , obtained from the fitted  $\tilde{J}_{\text{self}}(\omega)$  and  $\tilde{J}_{\text{cross}}(\omega)$  using Eq. 2 are shown for all three different signaling modes in Fig. 3.  $\tilde{T}_F(\omega)$  quantifies the system's response to all possible excitation frequencies. We find that for the entire frequency range, force transmission through the twist mode (blue) is the highest, followed by the shift mode (red) and the splay mode (green). From  $\text{Re } \tilde{T}_F(\omega)$  in Fig. 3, it is also evident that no force transmission is possible via the shift and splay mode for an input signal of frequency  $> 400$  GHz ( $\times 10^{-3} \text{ps}^{-1}$ ) and  $> 10$  GHz, respectively. These cutoff frequencies are similar to the water Debye mode at a frequency of about  $\simeq 20$  GHz [56], which suggests that the damping is partially due to the coupling to the hydration water. Except for the twist mode, the transmit functions are generally asymmetric, i.e., the sensor-to-effector side transmit function  $\tilde{T}_F^{s \rightarrow e}(\omega)$  and the effector-to-sensor side transmit function  $\tilde{T}_F^{e \rightarrow s}(\omega)$  are different. It should be noted that  $\tilde{T}_F(\omega)$  presented here characterizes the transmit properties of an isolated parallel CC. The effects of added sensor and effector protein modules can straightforwardly be obtained from the sensor and effector response functions using our previously developed convolution theory [57].

#### D. Signal transmission in the time domain

For practical purposes, signal transmission in the time domain needs to be characterized. The force transmit function in the time domain,  $T_F^{s \rightarrow e}(t)$ , is given by the inverse Fourier transform of  $\tilde{T}_F^{s \rightarrow e}(\omega)$  and describes the transmission of a  $\delta$ -function input force signal  $F_s(t)$  at the sensor side. Once  $T_F^{s \rightarrow e}(t)$  is known, the transmitted force  $F_e(t)$  at the effector side due to an arbitrary input force signal  $F_s(t)$  can be obtained via convolution

$$F_e(t) = \int_{-\infty}^t T_F^{s \rightarrow e}(\tau) F_s(t - \tau) d\tau. \quad (6)$$

$T_F(t)$  for the different signaling modes are shown in Fig. 4A, the method by which we obtain analytical representations for  $T_F(t)$  from  $\tilde{T}_F(\omega)$  is explained in *SI Appendix*, section 4. It is seen that the transmitted force signals for all the different modes decay rather quickly within 100 ps.

In reality, signals are not transmitted via infinitely short  $\delta$ -pulses but rather by pulses of finite duration.

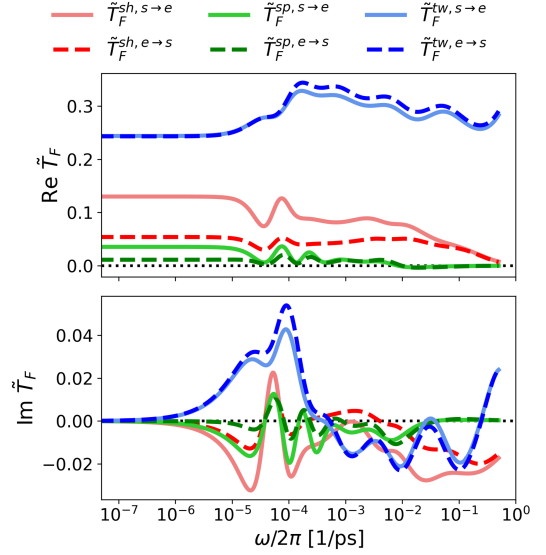


Figure 3. (top) Real and (bottom) imaginary part of force transmit functions  $\tilde{T}_F$  for the shift (sh), splay (sp), and twist (tw) modes of the CC obtained using analytical representations for the self and cross-response functions (details in *SI Appendix*, section 3) according to Eq. 2. The sensor-to-effector (s  $\rightarrow$  e) and effector-to-sensor (e  $\rightarrow$  s) transmit functions are shown as solid and dashed lines, respectively.

How efficiently the CC linker transmits such an input force signal depends on how quickly it responds to a suddenly imposed force and how quickly it relaxes back to its equilibrium state after the removal of force. To understand these complex dynamics, we discuss the transmitted output forces for input force step and rectangular force pulse,  $F_e^{\text{step}}(t)$  and  $F_e^{\text{rec}}(t)$ , both obtained from the convolution integral Eq. 6, for further details see *SI Appendix*, section 4. For a force switched on at  $t = 0$ ,  $F_e^{\text{step}}(t)$  is shown in Fig. 4B for the different modes. The transmitted force plateau values are reached for the different modes after 30–50 ns, which is around 2 orders of magnitude faster than the reported experimental timescale of  $2 \mu\text{s}$  associated with light-induced conformational transitions within the sensor module [17]. Signal transmission by all three modes would hence be sufficiently fast to not become time-limiting. The plateau value of  $F_e^{\text{step}}$  is the highest for the twist mode, followed by shift and splay modes. In Fig. 4C we present the transmitted force  $F_e^{\text{rec}}(t)$  for a rectangular force pulse signal of duration  $\tau = 1$  ns that is switched on at  $t = 0$ . It is seen that the transmitted force through each mode decay to zero within 40 ps after the removal of applied force. Results for different durations of the rectangular force pulse of  $\tau = 10^{-2}, 10^{-1}, 10^1, 10^2$  ns are presented in *SI Appendix* Fig. S4.

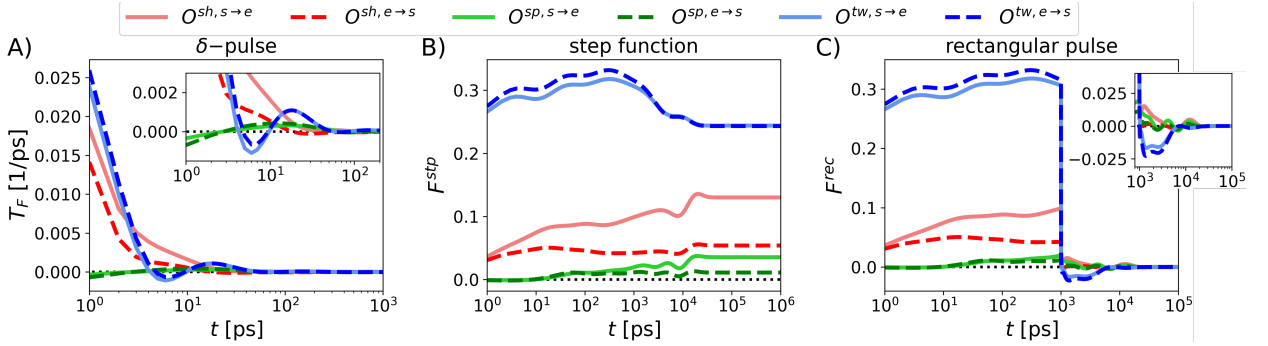


Figure 4. Transmitted force profiles for the different modes of the CC for different input force signals: A)  $\delta$  pulse, B) step function, and C) rectangular pulse of width  $\tau = 1$  ns. Insets in panel A and C represent zoomed-in force profiles. The force profiles in B and C are rescaled by the input force strength.

### E. Robustness with respect to mutations

It has been experimentally demonstrated that single-point mutations within the CC reduce the signal response of the blue-light-regulated histidine kinase YF1 [5, 53]. To study this in our framework, we perform MD simulations of two different experimentally studied mutants, Q133L, where Gln<sup>133</sup> is replaced by Leu, and R135L, where Arg<sup>135</sup> is replaced by Leu. We find that these single-point mutations do not affect the overall coiled-coil conformation, as seen from their different structural order parameter values compared with that of the wild-type CC in *SI Appendix*, Fig. S1. However, the dynamics and signaling response of these two mutants are completely different from each other and from the wild-type CC. For the mutant Q133L in Fig. 5A, the step force transmission for the shift and splay modes are negligible. Interestingly, the plateau value of the twist-mode in Fig. 5A is larger than that of the wild-type CC in Fig. 4B. Based on the absence of signaling for Q133L in experiments [5], this suggests that the signaling in the histidine kinase is not connected to the twist mode. For the mutant R135L in Fig. 5B, the plateau value of the shift-mode transmission is finite but negative, the splay-mode step transmission is much reduced, and the plateau value of the twist-mode transmission is almost half in comparison to the wild-type CC, in experiments the signaling activity is reduced but not absent [5]. In addition, structural characterization by electron paramagnetic resonance spectroscopy and X-ray solution scattering has revealed that light induces a splaying apart of the sensor domains and hence of the N-termini of the CC [17, 52]. Thus, by comparison with the experimental findings, we conclude that the signaling mode in the histidine kinase is predominantly of the splay type. Berntsson *et al.* [17] have experimentally observed superhelical coiling of the CC subsequent to its light-induced splaying, which suggests coupling be-

tween splay and twist deformations [50]. We quantify the coupling between different deformation modes by calculating the Pearson correlation coefficients (*Materials and Methods*) as summarized in Table I and indeed find significant splay-twist coupling which could explain the experimentally seen twisting by coupling to splay. We note that our simulations reveal that the twist mode is most stable with respect to mutations, so it is conceivable that the CC linker might in a different biological context also function as a twist transmitter.

Table I. Correlation coefficients between different deformation modes for the same ends (sensor and effector) and for different ends (cross).

type	sh-sp	sh-tw	sp-tw
sensor	-0.021	-0.012	-0.012
effector	0.26	-0.011	0.004
cross	-0.057	-0.006	0.006

### F. Transmission asymmetry

Asymmetry could possibly be important for the efficient information transfer from the sensor to the effector side. To look into this, we introduce the *rectification factor*  $\gamma$  as the ratio of sensor-to-effector ( $s \rightarrow e$ ) and effector-to-sensor ( $e \rightarrow s$ ) step-force transmission profile plateau values:

$$\gamma = \lim_{t \rightarrow \infty} \frac{F_e^{\text{stp}}(t)}{F_s^{\text{stp}}(t)}.$$

From the results in Fig. 4B we conclude that rectification for the splay mode is the highest,  $\gamma^{\text{sp}} = 3.2$ , followed by the shift mode,  $\gamma^{\text{sh}} = 2.4$ . In contrast, no rectification is observed for the twist mode, i.e.,

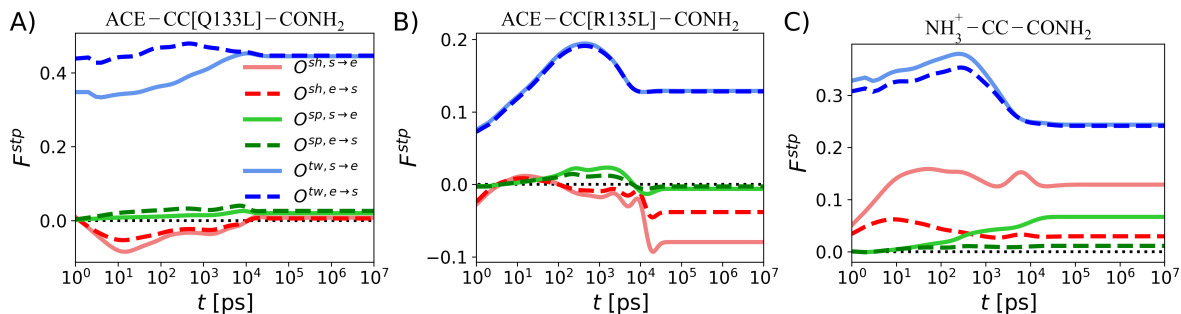


Figure 5. Comparison of transmitted force profiles for an input step force for modified CC systems: A,B) CC with different single-point mutations (Q133L or R135L) and C) CC with charged N-termini. All force profiles are rescaled by the input force strength. For a comparison with the wild-type CC with charge-neutral N and C-termini, see Fig. 4B.

$\gamma^{\text{tw}} = 1$ . These results can be rationalized by the fact that the rectification factor is given by the ratio of the real parts of the zero-frequency self responses for the sensor and the effector side, see *SI Appendix*, Fig. S3C. To study the relation between the rectification factor and the structural asymmetry in more detail, we introduce an additional asymmetry between the sensor and effector ends of the CC by uncapping the sensor-side  $\alpha$ -helix termini, which thereby become positively charged at neutral pH, resulting in the structure  $\text{NH}_3^+$ -CC-CONH<sub>2</sub> (note that the results presented in Figs. 1–4 are obtained for the CC linker with charge-neutral end groups: ACE-CC-CONH<sub>2</sub>). Though the step-force transmission profiles for ACE-CC-CONH<sub>2</sub> and  $\text{NH}_3^+$ -CC-CONH<sub>2</sub> are qualitatively the same, as follows by comparing Figs. 4B and 5C, we observe a pronounced difference of the plateau values for the  $s \rightarrow e$  and  $e \rightarrow s$  transmission for the shift and splay modes of  $\text{NH}_3^+$ -CC-CONH<sub>2</sub>. However, its  $s \rightarrow e$  and  $e \rightarrow s$  plateau values for the twist transmission are the same and remain unaffected in comparison to the charge neutral-termini system ACE-CC-CONH<sub>2</sub>. We thus find that the rectification factor can be tuned by changing the chemical structure of the sensor and effector terminal groups. It is tempting to relate the  $\gamma$  values for the different modes to their functional relevance, e.g., the highest value for  $\gamma^{\text{sp}}$  found here and the light-induced splaying of the CC linker observed in experiments [17, 52].

## DISCUSSION AND CONCLUSION

We introduce the theoretical framework to quantify the signal transmission between two distinct sites of a protein in terms of the associated self and cross response functions. The response functions are via the fluctuation–dissipation theorem related to equilibrium time-correlation functions, which can be generated from MD simulations but also from single-molecule experi-

ments. Note that in experiments, trajectories of separation coordinates typically include effects due to the coupling to measurement devices, which can be filtered out by using dynamic deconvolution theory [42, 58]. The displacement transmit function relates the correlations between two sites and the fluctuations at the site at which the input signal is applied, it thus quantifies the ratio of the output to the input signal and thus conveys more useful information than the often considered dynamic cross-correlation.

We apply our theoretical framework to the CC linker from the bacterial signaling protein YF1 and show that all three deformation modes, twist, shift and splay, achieve signal transfer from the sensor to the effector end of the CC. Although twist is in principle a better signal transmission mode, it does not conserve angular momentum and will therefore lead to a rotation of the sensor domain, this is probably why nature is not using it, at least for this protein construct. The experimentally observed splaying followed by superhelical coiling of the CC upon triggering [17] are expected due to a coupling between splay and twist deformation modes. Our analysis of simulation data for the wild-type CC and two important single-point mutants [53] suggests that splay is actually the signaling mode realized in the experimentally studied histidine kinase [17, 52].

Previous experiments have indicated that the length of the CC linker, not only the actual linker sequence, is instrumental in determining the response to light signals [55]. Our framework is directly applicable to study the CC length-dependent signaling. Moreover, our method will be useful to understand the dynamics of activation pathways of other cell signaling proteins with complex topology, e.g., G-protein-coupled receptors [59–61], which are the most frequent targets of drugs due to their involvement in diverse physiological processes. In this context it should be kept in mind that signal transmission through general protein networks can be predicted from the response functions of individual components

by repeated application of convolution relations for serial and parallel connections [42, 57]. Our study, thus, provides a way forward to relate atom-level protein dynamics to large-scale intermolecular communications of biological signaling networks.

Our theory is formulated at the linear-response level and thus is scale-invariant with respect to the input signal amplitude. In order to obtain the signal threshold beyond which the signal strength surpasses the noise background, one needs to compare the signal strength with the root-mean-square of the fluctuating force or displacement, similar to the definition of the signal-to-noise ratio in information theory [62]. We have in this paper only considered signaling between identical deformation modes at the two ends, i.e. twist to twist, splay to splay and shift to shift, off-diagonal signaling modes might be relevant experimentally and will be considered in future work.

## MATERIALS AND METHODS

### Models and force-field parameters

From the crystal structure of the whole signal transducing protein unit (PDB ID: 4GCZ), sensor (N-terminal) and effector (C-terminal) modules are deleted to obtain the structure of the CC linker [53]. The CC is composed of two parallel  $\alpha$ -helices each containing the same 23 residues ([126]Ile-Thr-Glu-His-Gln-Gln-Thr-Gln-Ala-Arg-Leu-Gln-Glu-Leu-Gln-Ser-Glu-Leu-Val-His-Val-Ser-Arg[148]). The CC is simulated in a rhombic dodecahedron box of volume  $227 \text{ nm}^3$  filled with 7135 water molecules (and counterions needed to neutralize the system). CHARMM36m protein force field parameters [63], the TIP3P water model [64, 65] and ion parameters from Ref. [66] are used. Four different systems with changes of N- and C-termini capping groups and/or a mutated residue are considered:  $\text{NH}_3^+-\text{CC}-\text{CONH}_2$ , ACE-CC-CONH<sub>2</sub>, ACE-CC[Q133L]-CONH<sub>2</sub>, ACE-CC[R135L]-CONH<sub>2</sub>. The acetyl (ACE) cap,  $\text{CH}_3\text{-CO-}$ , is used at the N-terminal and the “-CONH<sub>2</sub>” group is used at the C-terminal Arg, to simulate charge neutral termini. The two mutated systems are selected from the study by Gleichmann *et al.* [5].

### MD simulation details

For each system, a simulation is performed for  $20 \mu\text{s}$  in the  $NpT$  ensemble at temperature  $T = 300 \text{ K}$  and pressure  $p = 1 \text{ bar}$  with periodic boundary conditions using Gromacs 2020.1 [67]. The stochastic velocity rescaling thermostat [68] with a time constant

$\tau_T = 0.1 \text{ ps}$  is used to control temperature, while for pressure control an isotropic Parrinello–Rahman barostat [69] is used with a time constant  $\tau_p = 2 \text{ ps}$  and compressibility  $\kappa = 4.5 \times 10^{-5} \text{ bar}^{-1}$ . The LINCS algorithm [70] is used to constrain the bonds involving hydrogen atoms, allowing a timestep  $\Delta t = 2 \text{ fs}$ . Electrostatic interactions are computed using the particle mesh Ewald method [71] with a real-space cutoff distance of  $1.2 \text{ nm}$ , while van der Waals interactions are modeled using Lennard-Jones potentials with a cutoff distance of  $1.2 \text{ nm}$  where the resulting forces smoothly switch to zero between  $1 \text{ nm}$  to  $1.2 \text{ nm}$ . For the data analysis, simulation trajectories are saved every  $1 \text{ ps}$ . Images are rendered using the visual molecular dynamics (VMD) software [72]. Analysis is performed using in-house developed codes and Gromacs analysis modules [67]. Correlation functions for observable  $A(t)$  and  $B(t)$  are calculated as

$$C(\tau) = \frac{1}{L - \tau} \int_0^{L - \tau} A(t)B(t + \tau)dt = \langle A(t)B(t + \tau) \rangle,$$

where  $L$  is the trajectory length.

### Protein rotational relaxation time

The rotational relaxation time  $\tau_r$  of an object is related to the rotational diffusion coefficient as  $D_r = 1/2\tau_r$  and is estimated from the Stokes’ rotational diffusion coefficient  $D_r = k_B T / 8\pi\eta R_h^3$  [73]. Using the viscosity of the medium as that of water,  $\eta = 8.9 \times 10^{-1} \text{ Pa}\cdot\text{s}$ , and the hydrodynamic radius as half of the largest length scale of the full-length protein YF1,  $R_h = 7 \text{ nm}$ , we obtain  $\tau_r = 2 \mu\text{s}$  which exceeds the transmission relaxation times by far.

### Coupling between deformation modes

Pearson correlation coefficients between two different deformation modes are obtained as

$$R_{ij} = \frac{\langle (x_i - \langle x_i \rangle)(x_j - \langle x_j \rangle) \rangle}{\sqrt{\langle (x_i - \langle x_i \rangle)^2 \rangle} \sqrt{\langle (x_j - \langle x_j \rangle)^2 \rangle}},$$

where  $\langle \cdot \rangle$  denotes the time average and  $i, j$  refers to shift, splay or twist at the same ends or at different ends of the CC. The correlation coefficients  $R_{ij}$  for  $i \neq j$  (as  $R_{ii} = 1$ ) are summarized in Table I.

### Data, Materials, and Software Availability

All study data are included in the main text and/or *SI Appendix*. Derivations and additional figures that support the findings of this study are included in *SI Appendix*.



## ACKNOWLEDGEMENTS

We acknowledge funding by the European Research Council (ERC) Advanced Grant NoMaMemo Grant No.

835117, the Infosys foundation and computing time on the HPC cluster at ZEDAT, FU Berlin.

- 
- [1] T. Hunter, *Cell* **100**, 113 (2000).
- [2] R. G. Smock and L. M. Gierasch, *science* **324**, 198 (2009).
- [3] D. M. Rosenbaum, S. G. Rasmussen, and B. K. Kobilka, *Nature* **459**, 356 (2009).
- [4] M. P. Bhate, K. S. Molnar, M. Goulian, and W. F. DeGrado, *Structure* **23**, 981 (2015).
- [5] T. Gleichmann, R. P. Diensthuber, and A. Möglich, *Journal of Biological Chemistry* **288**, 29345 (2013).
- [6] S. J. Wodak, E. Paci, N. V. Dokholyan, I. N. Berezhovsky, A. Horovitz, J. Li, V. J. Hilser, I. Bahar, J. Karanicolas, G. Stock, *et al.*, *Structure* **27**, 566 (2019).
- [7] A. Cooper and D. Dryden, *European Biophysics Journal* **11**, 103 (1984).
- [8] G. M. Süel, S. W. Lockless, M. A. Wall, and R. Ranganathan, *Nature structural biology* **10**, 59 (2003).
- [9] J.-P. Changeux and S. J. Edelstein, *Science* **308**, 1424 (2005).
- [10] Q. Cui and M. Karplus, *Protein science* **17**, 1295 (2008).
- [11] H. N. Motlagh, J. O. Wrabl, J. Li, and V. J. Hilser, *Nature* **508**, 331 (2014).
- [12] R. Nussinov, C.-J. Tsai, and J. Liu, *Journal of the American Chemical Society* **136**, 17692 (2014).
- [13] V. A. Feher, J. D. Durrant, A. T. Van Wart, and R. E. Amaro, *Current opinion in structural biology* **25**, 98 (2014).
- [14] D. Thirumalai, C. Hyeon, P. I. Zhuravlev, and G. H. Lorimer, *Chemical reviews* **119**, 6788 (2019).
- [15] S. Brüschweiler, P. Schanda, K. Kloiber, B. Brutscher, G. Kontaxis, R. Konrat, and M. Tollinger, *Journal of the American Chemical Society* **131**, 3063 (2009).
- [16] J. Guo and H.-X. Zhou, *Chemical reviews* **116**, 6503 (2016).
- [17] O. Berntsson, R. P. Diensthuber, M. R. Panman, A. Björling, E. Gustavsson, M. Hoernke, A. J. Hughes, L. Henry, S. Niebling, H. Takala, *et al.*, *Nature communications* **8**, 1 (2017).
- [18] P. Mehrabi, E. C. Schulz, R. Dsouza, H. M. Müller-Werkmeister, F. Tellkamp, R. D. Miller, and E. F. Pai, *Science* **365**, 1167 (2019).
- [19] W. Y. Wahlgren, E. Claesson, I. Tuure, S. Trillo-Muyo, S. Bódizs, J. A. Ihalainen, H. Takala, and S. Westenhoff, *Nature Communications* **13**, 7673 (2022).
- [20] E. Lerner, T. Cordes, A. Ingargiola, Y. Alhadid, S. Chung, X. Michalet, and S. Weiss, *Science* **359**, eaan1133 (2018).
- [21] C. Schoeler, R. C. Bernardi, K. H. Malinowska, E. Durner, W. Ott, E. A. Bayer, K. Schulten, M. A. Nash, and H. E. Gaub, *Nano letters* **15**, 7370 (2015).
- [22] M. S. Bauer, F. Baumann, C. Daday, P. Redondo, E. Durner, M. A. Jobst, L. F. Milles, D. Mercadante, D. A. Pippig, H. E. Gaub, *et al.*, *Proceedings of the National Academy of Sciences* **116**, 6766 (2019).
- [23] O. Miyashita, J. N. Onuchic, and P. G. Wolynes, *Proceedings of the National Academy of Sciences* **100**, 12570 (2003).
- [24] W. Zheng, B. R. Brooks, and D. Thirumalai, *Proceedings of the National Academy of Sciences* **103**, 7664 (2006).
- [25] A. W. Van Wynsberghe and Q. Cui, *Structure* **14**, 1647 (2006).
- [26] K. Sharp and J. J. Skinner, *Proteins: Structure, Function, and Bioinformatics* **65**, 347 (2006).
- [27] H. T. Young, S. A. Edwards, and F. Gräter, *PLoS One* **8**, e64746 (2013).
- [28] T. Lenaerts, J. Ferkinghoff-Borg, F. Stricher, L. Serano, J. W. Schymkowitz, and F. Rousseau, *BMC structural biology* **8**, 1 (2008).
- [29] C. Chennubhotla and I. Bahar, *Molecular systems biology* **2**, 36 (2006).
- [30] A. Sethi, J. Eargle, A. A. Black, and Z. Luthey-Schulten, *Proceedings of the National Academy of Sciences* **106**, 6620 (2009).
- [31] C. F. Negre, U. N. Morzan, H. P. Hendrickson, R. Pal, G. P. Lisi, J. P. Loria, I. Rivalta, J. Ho, and V. S. Batista, *Proceedings of the National Academy of Sciences* **115**, E12201 (2018).
- [32] O. F. Lange and H. Grubmüller, *Proteins: Structure, Function, and Bioinformatics* **62**, 1053 (2006).
- [33] Y. Kong and M. Karplus, *Proteins: Structure, Function, and Bioinformatics* **74**, 145 (2009).
- [34] M. R. Mitchell, T. Tlusty, and S. Leibler, *Proceedings of the National Academy of Sciences* **113**, E5847 (2016).
- [35] J. Wang, A. Jain, L. R. McDonald, C. Gambogi, A. L. Lee, and N. V. Dokholyan, *Nature communications* **11**, 3862 (2020).
- [36] B. Buchli, S. A. Waldauer, R. Walser, M. L. Dönten, R. Pfister, N. Blöchliger, S. Steiner, A. Cafisch, O. Zerbe, and P. Hamm, *Proceedings of the National Academy of Sciences* **110**, 11725 (2013).
- [37] C. Viappiani, S. Abbruzzetti, L. Ronda, S. Bettati, E. R. Henry, A. Mozzarelli, and W. A. Eaton, *Proceedings of the National Academy of Sciences* **111**, 12758 (2014).
- [38] S. Buchenberg, F. Sittel, and G. Stock, *Proceedings of the National Academy of Sciences* **114**, E6804 (2017).
- [39] O. Bozovic, C. Zanobini, A. Gulzar, B. Jankovic, D. Buhrke, M. Post, S. Wolf, G. Stock, and P. Hamm, *Proceedings of the National Academy of Sciences* **117**, 26031 (2020).
- [40] O. Bozovic, J. Ruf, C. Zanobini, B. Jankovic, D. Buhrke, P. J. Johnson, and P. Hamm, *The Journal of Physical Chemistry Letters* **12**, 4262 (2021).

- [41] A. A. Ali, A. Gulzar, S. Wolf, and G. Stock, *The Journal of Physical Chemistry Letters* **13**, 9862 (2022).
- [42] M. Hinczewski, Y. von Hansen, and R. R. Netz, *Proceedings of the National Academy of Sciences* **107**, 21493 (2010).
- [43] R. Kubo, *Reports on progress in physics* **29**, 255 (1966).
- [44] A. N. Lupas and M. Gruber, *Advances in protein chemistry* **70**, 37 (2005).
- [45] P. Casino, V. Rubio, and A. Marina, *Current opinion in structural biology* **20**, 763 (2010).
- [46] V. Anantharaman, S. Balaji, and L. Aravind, *Biology direct* **1**, 1 (2006).
- [47] E. E. Matthews, M. Zoonens, and D. M. Engelman, *Cell* **127**, 447 (2006).
- [48] M. Hulko, F. Berndt, M. Gruber, J. U. Linder, V. Truffault, A. Schultz, J. Martin, J. E. Schultz, A. N. Lupas, and M. Coles, *Cell* **126**, 929 (2006).
- [49] M. Inouye, *Cell* **126**, 829 (2006).
- [50] A. Möglich, *Protein science* **28**, 1923 (2019).
- [51] A. Möglich, R. A. Ayers, and K. Moffat, *Journal of molecular biology* **385**, 1433 (2009).
- [52] O. Berntsson, R. P. Diensthuber, M. R. Panman, A. Björling, A. J. Hughes, L. Henry, S. Niebling, G. Newby, M. Liebi, A. Menzel, *et al.*, *Structure* **25**, 933 (2017).
- [53] R. P. Diensthuber, M. Bommer, T. Gleichmann, and A. Möglich, *Structure* **21**, 1127 (2013).
- [54] A. V. Oppenheim, A. S. Willsky, and S. H. Nawab, *Signals & Systems*, 2nd ed. (Prentice-Hall, Upper Saddle River, NJ, 1996).
- [55] R. Ohlendorf, C. H. Schumacher, F. Richter, and A. Möglich, *ACS synthetic biology* **5**, 1117 (2016).
- [56] K. F. Rinne, J. C. Schulz, and R. R. Netz, *The Journal of Chemical Physics* **142** (2015).
- [57] Y. von Hansen, S. Rode, and R. R. Netz, *The European Physical Journal E* **36**, 1 (2013).
- [58] Y. von Hansen, A. Mehlich, B. Pelz, M. Rief, and R. R. Netz, *Review of Scientific Instruments* **83** (2012).
- [59] D. M. Thal, A. Glukhova, P. M. Sexton, and A. Christopoulos, *Nature* **559**, 45 (2018).
- [60] D. Hilger, M. Masureel, and B. K. Kobilka, *Nature structural & molecular biology* **25**, 4 (2018).
- [61] I. Rodríguez-Espigares, M. Torrens-Fontanals, J. K. Tiemann, D. Aranda-García, J. M. Ramírez-Angueta, T. M. Stepniewski, N. Worp, A. Varela-Rial, A. Morales-Pastor, B. Medel-Lacruz, *et al.*, *Nature Methods* **17**, 777 (2020).
- [62] D. J. MacKay, *Information theory, inference and learning algorithms* (Cambridge university press, 2003).
- [63] J. Huang, S. Rauscher, G. Nawrocki, T. Ran, M. Feig, B. L. De Groot, H. Grubmüller, and A. D. MacKerell, *Nature methods* **14**, 71 (2017).
- [64] W. L. Jorgensen, J. Chandrasekhar, J. D. Madura, R. W. Impey, and M. L. Klein, *The Journal of chemical physics* **79**, 926 (1983).
- [65] A. D. MacKerell Jr, D. Bashford, M. Bellott, R. L. Dunbrack Jr, J. D. Evanseck, M. J. Field, S. Fischer, J. Gao, H. Guo, S. Ha, *et al.*, *The journal of physical chemistry B* **102**, 3586 (1998).
- [66] R. M. Venable, Y. Luo, K. Gawrisch, B. Roux, and R. W. Pastor, *The journal of physical chemistry B* **117**, 10183 (2013).
- [67] M. J. Abraham, T. Murtola, R. Schulz, S. Páll, J. C. Smith, B. Hess, and E. Lindahl, *SoftwareX* **1**, 19 (2015).
- [68] G. Bussi, D. Donadio, and M. Parrinello, *The Journal of chemical physics* **126**, 014101 (2007).
- [69] M. Parrinello and A. Rahman, *Journal of Applied physics* **52**, 7182 (1981).
- [70] B. Hess, H. Bekker, H. J. Berendsen, and J. G. Fraaije, *Journal of computational chemistry* **18**, 1463 (1997).
- [71] T. Darden, D. York, and L. Pedersen, *The Journal of chemical physics* **98**, 10089 (1993).
- [72] W. Humphrey, A. Dalke, and K. Schulten, *Journal of molecular graphics* **14**, 33 (1996).
- [73] L. D. Landau and E. M. Lifshitz, *Fluid Mechanics: Landau and Lifshitz: Course of Theoretical Physics, Volume 6*, Vol. 6 (Elsevier, 2013).

# Supporting Information for

## Quantifying the efficiency of principal signal transmission modes in proteins

Anil Kumar Sahoo, Richard Schwarzl, Markus S. Miettinen, Roland R. Netz

arXiv:2403.12312v1 [cond-mat.soft] 18 Mar 2024

## SUPPORTING INFORMATION TEXT

### 1. Order parameters for characterizing the coiled-coil (CC) structure

*Fraction of native contacts*,  $Q$ , is defined as [1]:

$$Q(t) = \frac{1}{N_c} \sum_{(i,j)} \frac{1}{1 + \exp\{\lambda[r_{ij}(t) - \nu r_{ij}^0]\}},$$

where the sum runs over  $N_c$  pairs of native contacts  $(i, j)$ ,  $r_{ij}(t)$  is the distance between  $i$  and  $j$  at time  $t$ ,  $r_{ij}^0$  is the distance between  $i$  and  $j$  in the native structure of the protein,  $\lambda$  ( $= 5 \text{ \AA}^{-1}$ ) is a smoothening parameter, and  $\nu$  ( $= 1.8$ ) takes care of the fluctuations during contact formation. Here, the list of native contact pairs  $(i, j)$  is constructed by considering all pairs of heavy atoms belonging to residues  $R_i$  and  $R_j$  such that  $|R_i - R_j| > 3$  and the distance between  $i$  and  $j$  is less than  $4.5 \text{ \AA}$ .

*Root-mean-square deviation*, RMSD, in distances is defined as

$$RMSD(t) = \sqrt{\frac{1}{N} \sum_{i=1}^N |r_i(t) - r_i^0|^2},$$

where  $N$  is the total number of heavy atoms of the CC,  $r_i(t)$  is the position of the  $i^{\text{th}}$  atom at time  $t$ , and  $r_i^0$  is the position of the same atom in the native structure of the CC.

*Secondary structure*, SS, contents of the CC are calculated by the STRIDE algorithm [2] implemented in the VMD software [3]. The fraction of SS content is defined as the ratio of the number of residues of the protein involved in  $\alpha$ -helical SS formation at time  $t$  to that in the native structure of the CC.

### 2. Force transmission through a viscous bead–spring model

To illustrate force transmission through a model signal transmitter, we consider a simple viscoelastic model: two beads with different mobilities  $\mu_s$  (sensor) and  $\mu_e$  (effector) that are connected by a harmonic spring of stiffness  $k$ , similar to Fig. 1B in the main text [4]. Under the application of oscillating forces with amplitudes  $f_s(\omega)$  and  $f_e(\omega)$  to the sensor and the effector,

respectively, the Fourier-transformed sensor velocity is given by  $-i\omega\tilde{x}_s(\omega) = \mu_s(f_s(\omega) + k[\tilde{x}_e(\omega) - \tilde{x}_s(\omega)])$ , whereas the effector velocity is given by  $-i\omega\tilde{x}_e(\omega) = \mu_e(f_e(\omega) + k[\tilde{x}_s(\omega) - \tilde{x}_e(\omega)])$ . Using the definitions of linear response functions from Eq. 1 in the main text, we obtain

$$\tilde{J}_{\text{self}}^s = \frac{\mu_s(\omega + i\mu_e k)}{\omega(\mu k - i\omega)}, \quad \tilde{J}_{\text{self}}^e = \frac{\mu_e(\omega + i\mu_s k)}{\omega(\mu k - i\omega)}, \quad \tilde{J}_{\text{cross}} = \frac{i\mu_s\mu_e k}{\omega(\mu k - i\omega)}, \quad (\text{S1})$$

where  $\mu = \mu_s + \mu_e$ . The force transmission from the sensor to the effector side is determined according to Eq. 2 in the main text as

$$\tilde{T}_{\text{F}}^{\text{s}\rightarrow\text{e}}(\omega) = \frac{\tilde{J}_{\text{cross}}(\omega)}{\tilde{J}_{\text{self}}^e(\omega)} = \frac{\mu_s k}{(\mu_s k - i\omega)}. \quad (\text{S2})$$

Note that  $\tilde{T}_{\text{F}}^{\text{s}\rightarrow\text{e}}$  is independent of the effector side bead mobility, and at zero frequency, which corresponds to the long-time limit, the force transmission is given by  $\tilde{T}_{\text{F}}^{\text{s}\rightarrow\text{e}} = 1$ . The derived force transmit function has the same form as the Debye function. For more realistic force transducers, such as proteins,  $\tilde{T}_{\text{F}}$  can be expressed as a sum of Debye functions that reflect the normal modes of a protein.

### 3. Fitting procedure for the analytical representation of a response function

We consider multi-exponential functions for fitting the response function  $J(t)$  according to

$$J(t) = \theta(t) \sum_{k=1}^N c_k e^{-t/\tau_k} = \sum_{k=1}^N g_k(t), \quad (\text{S3})$$

where  $\theta$  is the Heaviside step function given by

$$\theta(t) = \begin{cases} 1 & t \geq 0 \\ 0 & t < 0. \end{cases}$$

The Fourier transform of a single-sided exponential is the Debye function given by

$$\tilde{g}_k(\omega) = \frac{c_k}{\tau_k^{-1} + i\omega} = \frac{c_k \tau_k}{1 + \tau_k^2 \omega^2} - i \frac{c_k \tau_k^2 \omega}{1 + \tau_k^2 \omega^2}. \quad (\text{S4})$$

The real part of the fit function is given by

$$\text{Re} [\tilde{J}(\omega)] = \text{Re} \left[ \sum_{k=1}^N \tilde{g}_k(\omega) \right] = \sum_{k=1}^N \frac{c_k \tau_k}{1 + \tau_k^2 \omega^2} \quad (\text{S5})$$

and the imaginary part is given by

$$\text{Im} [\tilde{J}(\omega)] = \text{Im} \left[ \sum_{k=1}^N \tilde{g}_k(\omega) \right] = - \sum_{k=1}^N \frac{c_k \tau_k^2 \omega}{1 + \tau_k^2 \omega^2}. \quad (\text{S6})$$

Eqs. S5,S6 are used to simultaneously fit the real and imaginary part of the Fourier-transformed response functions. Logarithmically-spaced frequency data are taken for the fitting. The time constants  $\tau_k$  in Eq. S3 are restricted to positive values only. The number of Debye functions,  $N$ , used for fitting the self and cross-response functions for the different systems are given in Table S1. Such fits for the twist mode and the shift and splay modes of the ACE-CC-CONH<sub>2</sub> system are shown in Figs. 2C,D in the main text and S3C,D, respectively. Importantly, we find that the parameters  $c_k$  and  $\tau_k$  obtained from the frequency-domain fitting accurately reproduce the simulated time-domain response functions, validating the robustness of our fitting procedure (see Figs. 2B in the main text and S3B).

Table S1. Number of Debye relaxation functions  $N$  used for fitting self and cross-response functions for the different systems.

System	$N(\tilde{J}_{\text{self}})$	$N(\tilde{J}_{\text{cross}})$
ACE-CC-CONH <sub>2</sub>	10	10
NH <sub>3</sub> <sup>+</sup> -CC-CONH <sub>2</sub>	7	10
ACE-CC[Q133L]-CONH <sub>2</sub>	7	10
ACE-CC[R135L]-CONH <sub>2</sub>	7	10

#### 4. Time-domain transmit function from the analytical form of $\tilde{T}_{\text{F}}(\omega)$ via partial fraction decomposition

The time-domain force transmit function,  $T_{\text{F}}(t)$ , corresponds to the system response to a  $\delta$ -function input pulse and is given by the inverse Fourier transform of the Fourier-domain transmit function,  $\tilde{T}_{\text{F}}(\omega)$ , according to  $T_{\text{F}}(t) = \frac{1}{2\pi} \int_{-\infty}^{+\infty} \tilde{T}_{\text{F}}(\omega) e^{i\omega t} d\omega$ . Instead of using a numerical discrete Fourier transform, we obtain  $T_{\text{F}}(t)$  from  $\tilde{T}_{\text{F}}(\omega)$  analytically as follows. Since all response functions  $\tilde{J}(\omega)$  are expressed as sums of Debye functions (see Section 3), the Fourier-transformed force

transmit function is given by

$$\tilde{T}_F(\omega) = \frac{\tilde{J}_{\text{cross}}(\omega)}{\tilde{J}_{\text{self}}(\omega)} = \sum_{j=1}^M \frac{a_j}{\alpha_j + i\omega} \bigg/ \sum_{k=1}^N \frac{b_k}{\beta_k + i\omega}, \quad (\text{S7})$$

where  $a_j$ ,  $\alpha_j$ ,  $b_k$ , and  $\beta_k$  are the fitting parameters. The above expression can be rewritten as a sum of Debye functions using partial fraction decomposition as

$$\tilde{T}_F(\omega) = c_0 + \sum_{l=1}^Q \frac{c_l}{\gamma_l + i\omega}, \quad (\text{S8})$$

where  $c_0$ ,  $c_l$ , and  $\gamma_l$  are uniquely determined parameters. Based on Eq. S8 the analytical inverse Fourier transform is obtained as

$$T_F(t) = c_0\delta(t) + \theta(t) \sum_{l=1}^Q c_l e^{-\gamma_l t}, \quad (\text{S9})$$

where  $\theta(t)$  is the Heaviside step function.

Once the transmit function  $T_F(t)$  is known, the transmitted force  $F_e(t)$  at the effector site follows from the input force  $F_s(t)$  at the sensor site by convolution. For a step input force signal  $F_s(t) = F_0\theta(t)$  we obtain

$$\begin{aligned} F_e^{\text{stp}}(t) &= F_0 \int_{-\infty}^{\infty} T_F(t')\theta(t-t')dt' = F_0 \int_{-\infty}^t T_F(t')dt' \\ \implies F_e^{\text{stp}}(t)/F_0 &= c_0\theta(t) + \sum_{l=1}^Q \frac{c_l}{\gamma_l} (1 - e^{-\gamma_l t}). \end{aligned} \quad (\text{S10})$$

Similarly, the rectangular pulse response is given by

$$F_e^{\text{rec}}(t) = F_0 \int_{-\infty}^{\infty} T_F(t')\Pi(t-t')dt',$$

where  $\Pi(t)$  is a rectangular pulse of width  $\tau$  defined as

$$\Pi(t) = \begin{cases} 0 & t < 0 \\ 1 & 0 \leq t \leq \tau \\ 0 & t > \tau. \end{cases}$$

The above convolution integral is evaluated to be:

$$F_e^{\text{rec}}(t)/F_0 = \begin{cases} \int_0^t T_F(t')dt' & 0 \leq t \leq \tau \\ \int_{t-\tau}^t T_F(t')dt' & t > \tau \end{cases} = \begin{cases} c_0 + \sum_{l=1}^Q \frac{c_l}{\gamma_l} (1 - e^{-\gamma_l t}) & 0 \leq t \leq \tau \\ \sum_{l=1}^Q \frac{c_l}{\gamma_l} e^{-\gamma_l t} (e^{\gamma_l \tau} - 1) & t > \tau. \end{cases} \quad (\text{S11})$$

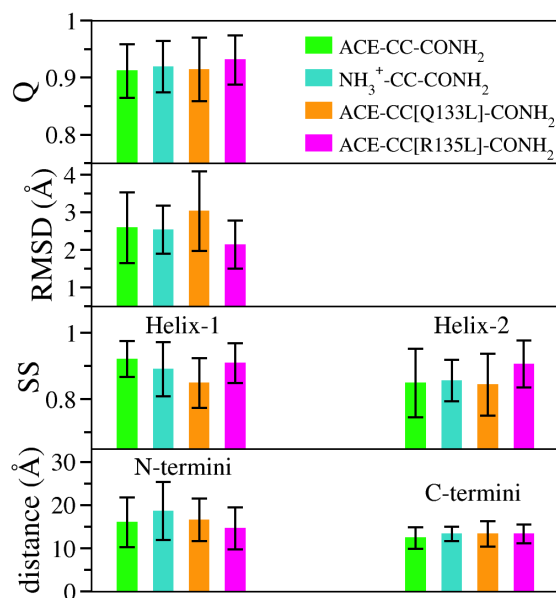


Figure S1. Average values of different structural order parameters for the four simulated coiled-coil systems: ACE-CC-CONH<sub>2</sub>, NH<sub>3</sub><sup>+</sup>-CC-CONH<sub>2</sub>, ACE-CC[Q133L]-CONH<sub>2</sub>, and ACE-CC[R135L]-CONH<sub>2</sub>. See Section 1 for the definitions of the order parameters. The results demonstrate that all four systems are stable over the total simulation time of 20  $\mu$ s each.



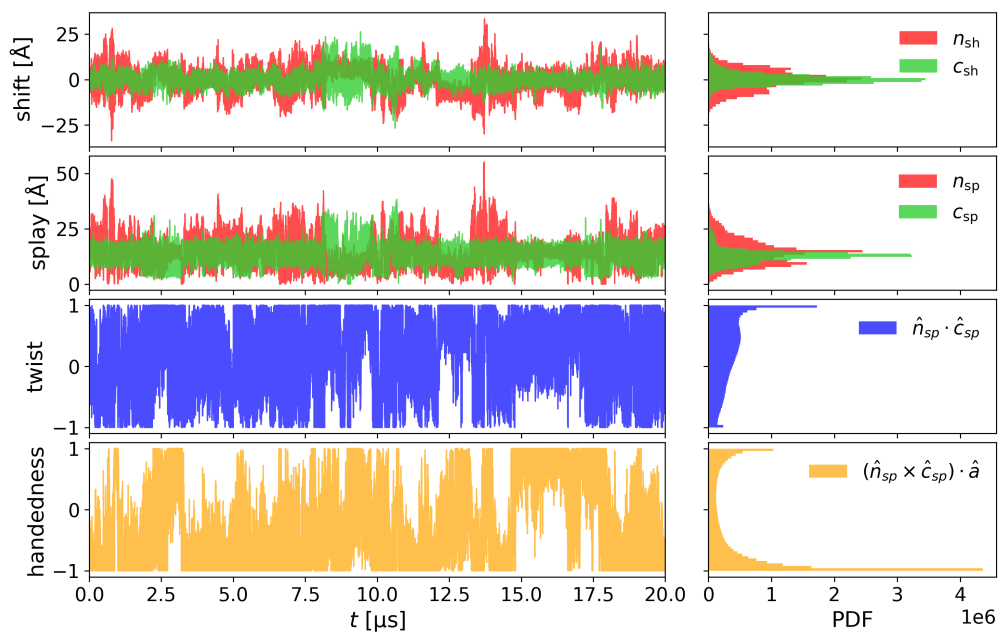


Figure S2. Time series and corresponding probability distribution functions for the shift, the splay, the cosine of the twist angle between N and C termini, and the handedness of the rotation of the coiled coil along its long-axis  $\vec{a}$ , defined as  $(\hat{n}_{sp} \times \hat{c}_{sp}) \cdot \hat{a}$ . See Fig. 1 and the main text for the definitions of shift, splay, and the twist angle. Results are shown for the wild-type coiled coil with capped neutral termini (ACE-CC-CONH<sub>2</sub>).

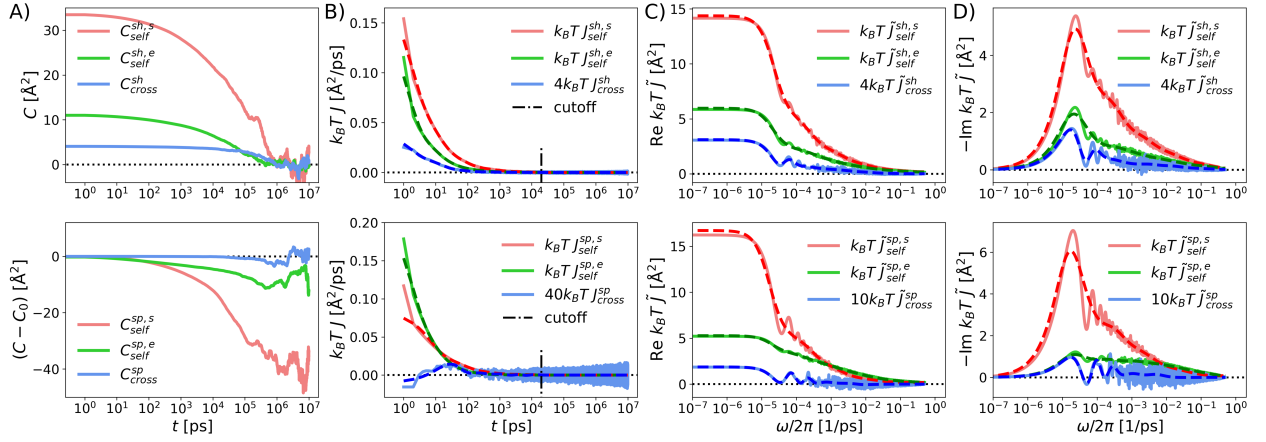


Figure S3. Results for the shift (top) and splay modes (bottom) of the wild-type coiled coil with capped neutral termini (ACE-CC-CONH<sub>2</sub>). A) Self and cross-correlation functions  $C_{\text{self}}$  and  $C_{\text{cross}}$ . For the splay mode, we subtract  $C_0 = C(t = 0)$  in order to be able to compare all correlation functions in one plot. B) Response functions  $J(t)$ , obtained from the numerical time-derivatives of the correlation functions, are shown as solid lines. The vertical dash-dotted lines represent the cutoff beyond which the response functions are set to zero to prevent noise artifacts when calculating Fourier transforms. C) Real and D) imaginary parts of  $\tilde{J}(\omega)$  obtained from discrete fast-Fourier transformation of the time-domain response function  $J(t)$ , shown as solid lines. Dashed lines represent simultaneous fits to the logarithmically-spaced real and imaginary parts of  $\tilde{J}(\omega)$  by a sum of 10 Debye functions, for further details, see Section 3. Dashed lines in panel B represent the inverse Fourier transform of the fits in C and D. Note that the cross response functions in B, C, and D are multiplied with different scaling factors for a better visualization.

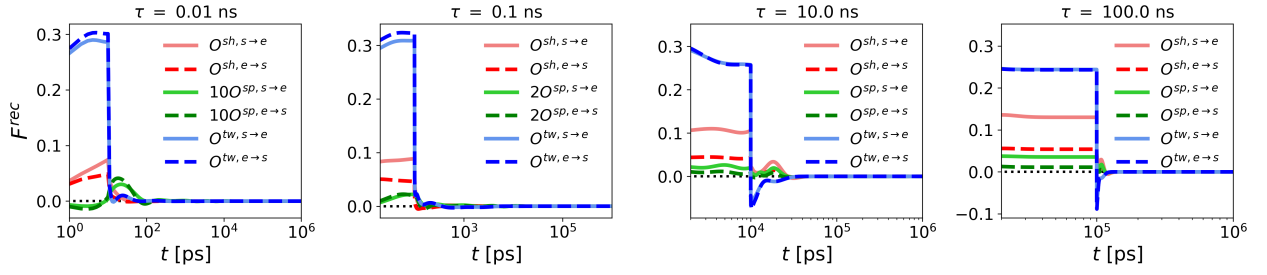


Figure S4. Transmitted force profiles for rectangular pulse force input for shift, splay, and twist modes of the wild-type coiled coil with capped neutral termini (ACE-CC-CONH<sub>2</sub>) for different input pulse widths  $\tau$  given on the top of each plot. Note that for the splay mode, transmitted force profiles are multiplied with a different scaling factor in each plot for a better visualization.

- 
- [1] R. B. Best, G. Hummer, and W. A. Eaton, *Proceedings of the National Academy of Sciences* **110**, 17874 (2013).
- [2] D. Frishman and P. Argos, *Proteins: Structure, Function, and Bioinformatics* **23**, 566 (1995).
- [3] W. Humphrey, A. Dalke, and K. Schulten, *Journal of molecular graphics* **14**, 33 (1996).
- [4] M. Hinczewski, Y. von Hansen, and R. R. Netz, *Proceedings of the National Academy of Sciences* **107**, 21493 (2010).